We are IntechOpen, the world's leading publisher of Open Access books Built by scientists, for scientists

6,900
Open access books available

185,000
International authors and editors

200M
Downloads

Our authors are among the

154
Countries delivered to

TOP 1%
most cited scientists

12.2%
Contributors from top 500 universities



WEB OF SCIENCE™

Selection of our books indexed in the Book Citation Index in Web of Science™ Core Collection (BKCI)

Interested in publishing with us?
Contact book.department@intechopen.com

Numbers displayed above are based on latest data collected.
For more information visit www.intechopen.com



Chapter 8

Characterization and Simulation of p-Type Ion Implantation in MCT

Changzhi Shi

Additional information is available at the end of the chapter

http://dx.doi.org/10.5772/intechopen.77111

Abstract

Ion implantation is one of the key technologies for the fabrication of HgCdTe (MCT) infrared photodiodes. In order to achieve p-on-n type photodiode structure with better performance, the group V elements typically serve as p-type dopants, especially arsenic. In this chapter, ion profiles, defect microstructures, and surface amorphization of implanted group V dopants represented by arsenic into MCT epilayers were characterized by secondary ion mass spectroscopy (SIMS), transmission electron microscopy (TEM), and X-ray diffraction (XRD), respectively. The influences of some significant technological parameters related to ion implantation, such as implant energy, implant dose, ion beam current, barrier layer structure, on the distributions of ions and induced damages are analyzed. In addition, the high-temperature annealing used to eliminate induced damages and activate the electrical activity of ions was subjected to the as-implanted samples, and the ion diffusion profiles and surface microstructures were acquired and analyzed. Finally, the computer simulations on the collision of incident ions and lattice atoms were carried out to study the distributions of ions and recoil atoms numerically. The simulation results are in good agreement with the experimental data.

Keywords: HgCdTe, ion implantation, group V, microscopic characterization, computer simulation, SIMS, TEM, XRD

1. Introduction

In the field of semiconductor and microelectronics, the ion implantation process is the most common technology applied to incorporate dopants. Compared with the other two methods, such as thermal diffusion doping and epitaxy in-situ doping, the ion implantation has

IntechOpen

© 2018 The Author(s). Licensee IntechOpen. This chapter is distributed under the terms of the Creative Commons Attribution License (http://creativecommons.org/licenses/by/3.0), which permits unrestricted use, distribution, and reproduction in any medium, provided the original work is properly cited. CC BY

the advantages of simple process, depth controllability, selective and arbitrary concentration doping (not restricted by solid solubility). For MCT, an important narrow gap semiconductor material applied in the field of infrared detection and imaging [1], ion implantation and in-situ epitaxy are both adopted for the incorporation of dopants. In fact, the core element of MCT-based infrared detectors is typically a photodiode based on p-n junction structure, generating a photogenerated potential under the excitation of infrared photons. The p-n junction can be formed either on the p-type absorbing layer or on the n-type absorbing layer, corresponding to n-on-p device [2, 3] and p-on-n device [4], respectively. In the traditional n-on-p device, the in-situ p-type doping can be achieved by Hg vacancy doping [5] and Au or Cu incorporation [6] during epitaxy growth; the n-type doping can be acquired by boron ion implantation. With decades of development, the n-on-p device has provided excellent performance [7]. However, for the infrared detection application of low dark current and low flux in long wavelength infrared (LWIR) and very long wavelength infrared (VLWIR) regions, the p-on-n device has been demonstrated to possess better performances [8–10] such as low dark current, low series resistance, and high operating temperature. For II-VI materials such as MCT, group V elements, especially arsenic, can serve as p-type dopants. Due to its low diffusion coefficient [8] in MCT, the profiles of implanted arsenic ions can be controllable. So far, arsenic has been extensively used as the p-type dopant of MCT. Nevertheless, the implanted arsenic ions usually occupy the cation sublattice and generate a large number of induced damages. Therefore, a high-temperature annealing is necessary to eliminate lattice damages and activate the electrical activity of arsenic ions, that is, transfer arsenic ions from cation sublattices to Te sublattices.

Some studies on arsenic ion implantation in MCT have been reported in several literature studies [4, 8, 11] and our previous work [12–14]. Classically, SIMS is used to acquire the distribution profiles of implanted ions, while the microstructures and distributions of induced damages are observed by TEM. Recently, Rutherford backscattering experiments under channeling conditions (RBS-c) were carried out to extract quantitative damage depth profiles of implanted arsenic ions in MCT [15]. Moreover, the microstructures of the induced damages in the MCT implanted with group V dopants (N, P, As and Sb) were investigated [16]. However, so far, the systematic study on the ion implantation of group V dopants in MCT has not been reported. Therefore, in this chapter, the ion implantation of group V dopants, such as P, As, Sb, in MCT will be analyzed and discussed according to characterization methods. Finally, the computer simulations on the collision of incident ions and lattice atoms will be carried out to study the distributions of ions and recoil atoms numerically.

2. SIMS profile

SIMS is a high-resolution analytic technique for acquiring the element component information in the material. In this section, the depth profiles of group V dopants implanted into MCT will be characterized by this method.

2.1. Arsenic

The technological parameters of ion implantation, such as implant energy, implant dose, ion beam current, determine the depth profiles of implanted ions and induced damages. In order to implant heavy ions like arsenic into MCT epilayer, the implant energy should be adequately high to overcome the energy loss in the collision of implant ions and lattice atoms. Here, the MCT epilayers were grown on (111)B CdZnTe substrates by liquid phase epitaxy (LPE). Then, arsenic ions were implanted into MCT epilayers without barrier layers. **Figure 1** provides the SIMS profiles of arsenic ions implanted into MCT at different implant energies before and after high-temperature annealing under saturated Hg vapor pressure. The energy ranges from 350 to 450 keV, while the dose is set to be 2×10^{14} cm^{-2}. The high-temperature annealing was carried out in two steps: the first step at 420°C is used to transfer arsenic ions from cation sublattices to Te sublattices and eliminate induced damages, while the second step at 240°C is to remove Hg vacancies. It can be seen from **Figure 1** that the depth of the end-of-range (EOR) of as-implanted arsenic ions increases with implant energy. Moreover, the average projected range (Rp) increases approximately linearly with energy. After annealing, the indiffusion occurs to the as-implanted arsenic ions, and the diffusion depth also increases with energy.

In addition to implant energy, implant dose is also one of the key technological parameters determine the distribution of implanted ions. The SIMS profiles of the arsenic ions implanted into MCT epilayers without barrier layers at 320 keV with different doses are illustrated in **Figure 2(a)**. The peak concentration of arsenic ions increases with dose; however, the EOR depth is not remarkably influenced by implant dose. **Figure 2(b)** provides the SIMS profiles of as-implanted arsenic ions in MCT with the dose of 5×10^{14} cm^{-2} after Hg overpressure annealing. The profile indicates that the indiffusion of arsenic ions includes three parts: part 1 – in the surface layer, it is considered that the arsenic ions are trapped by the defects in the lattice, thereby resulting in the generation of arsenic complexing; part 2 – beneath the surface layer, the arsenic ions are diffused thermally into the lattice and some of them are activated electrically

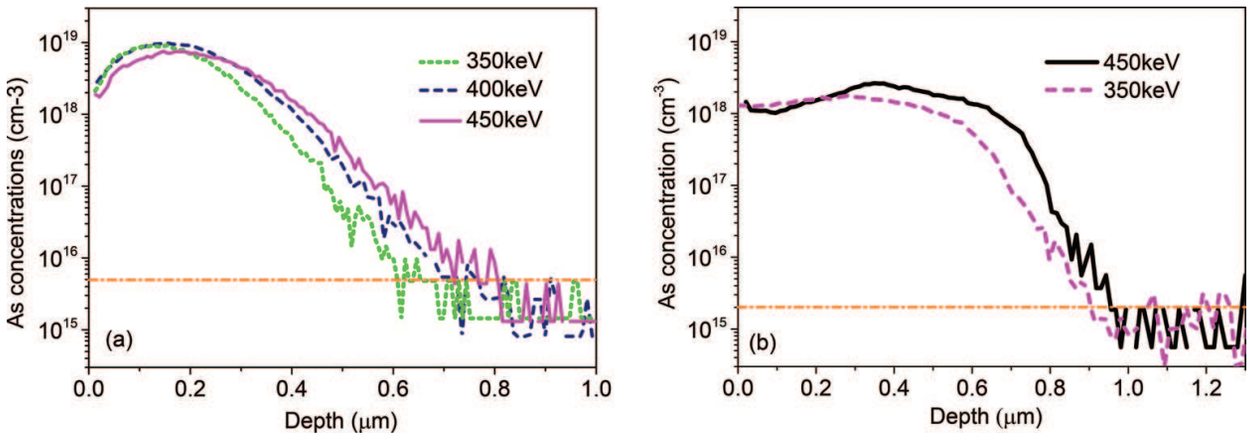


Figure 1. SIMS profiles of arsenic ions implanted into MCT at different energies: (a) before Hg overpressure annealing and (b) after Hg overpressure annealing.

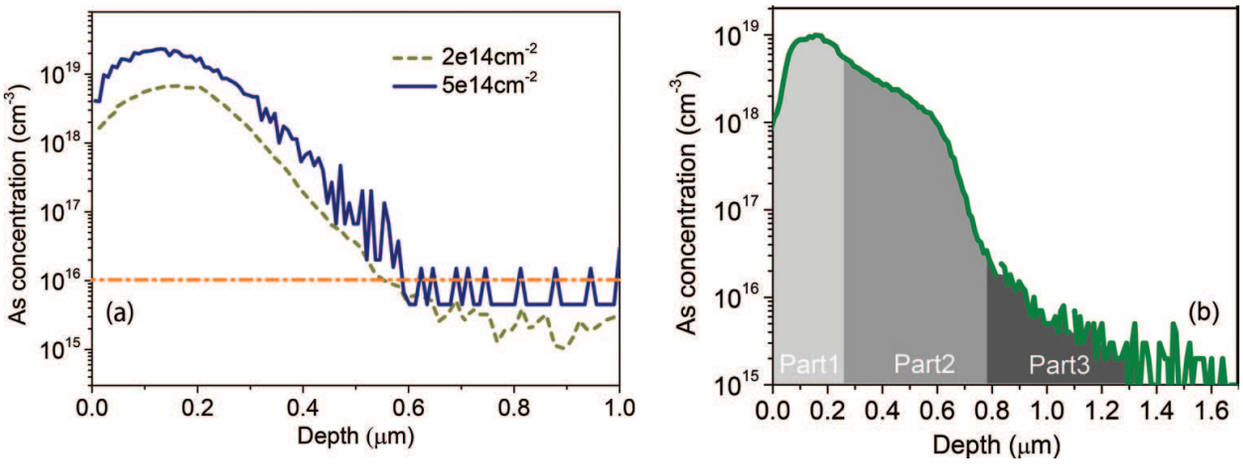


Figure 2. (a) SIMS profiles of arsenic ions implanted into MCT at 320 keV with the doses of 2×10^{14} and 5×10^{14} cm^{-2}, respectively. (b) SIMS profile of arsenic ions in the annealed MCT implanted at 320 keV with the dose of 5×10^{14} cm^{-2}.

by occupying Te sublattices; part 3 – deeper in lattice, there exists a rapid diffusion of arsenic ions due to the channeling effect. This profile is similar to the profiles presented in Refs. [4, 8]. However, the multicomponent indiffusion does not occur to the annealed samples with lower dose as shown in **Figure 1**. It could be due to that the dose of the samples in **Figure 1** is lower than that of the sample in **Figure 2**. It implies that the high dose may aggravate the complexing and the channeling effect of as-implanted arsenic ions.

The ion beam current is another technological parameter to be considered. **Figure 3(a)** shows the SIMS profiles of arsenic ions implanted into MCT epilayers without barrier layers at 320 keV with the dose of 5×10^{14} cm^{-2}, at the beam currents of 100 μA and 300 μA, respectively. It can be seen that the ion profiles are not sensitive to the beam current for arsenic. Even when the span of the beam current is expanded to 50–800 μA, no significant distinction in the ion profiles could be found in **Figure 3(b)**. **Figure 4** provides the SIMS profiles of arsenic ions in the samples in **Figure 3(a)** annealed under saturated Hg vapor pressure. Although the arsenic

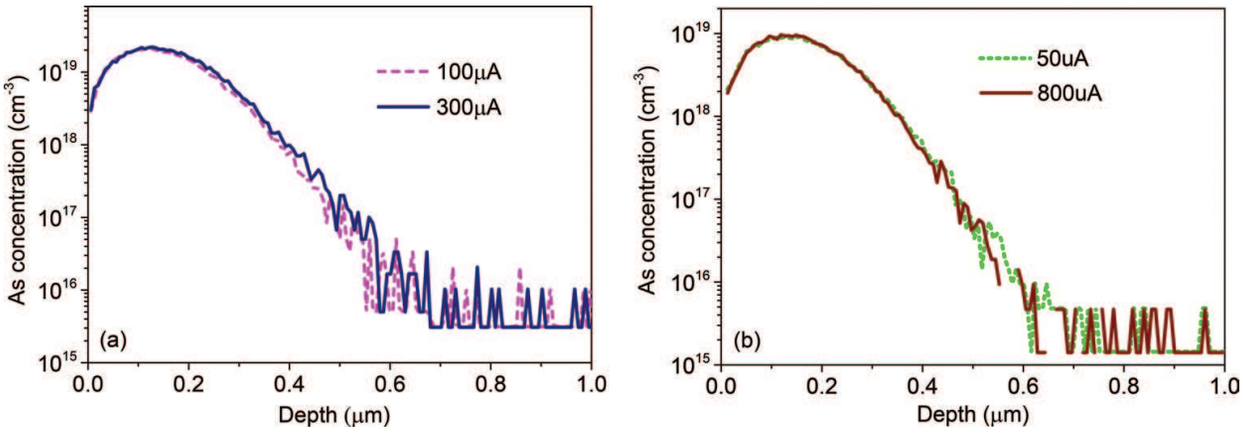


Figure 3. (a) SIMS profiles of arsenic ions implanted into MCT epilayers at 320 keV with the dose of 5×10^{14} cm^{-2}, at the beam currents of 100 and 300 μA, respectively. (b) SIMS profiles of arsenic ions implanted into MCT epilayers at 350 keV with the dose of 2×10^{14} cm^{-2}, at the beam currents of 50 and 800 μA, respectively.

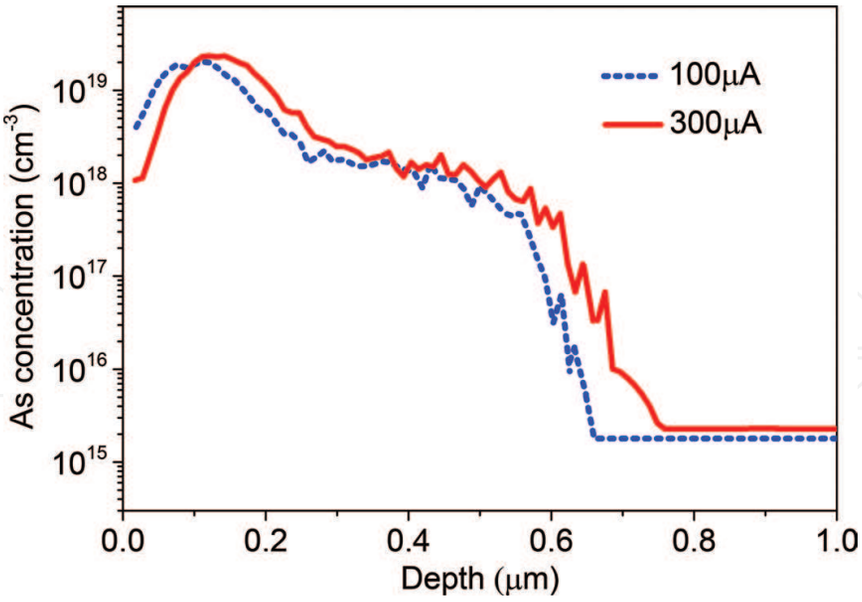


Figure 4. SIMS profiles of arsenic ions in the annealed MCT samples implanted at 320 keV with the dose of 5×10^{14} cm^{-2}, at the beam currents of 100 and 300 μA, respectively.

profiles in the as-implanted samples are sensitive to beam current, the sample with higher beam current presents a deeper diffusion depth than that of the sample with lower beam current. It indicates that the change in beam current gives rise to the different distributions of induced damages, thereby influencing the indiffusion of arsenic ions.

The distribution profiles of as-implanted arsenic ions in bare MCT are discussed above. Nevertheless, in the practical device fabrication, the barrier layers should be prepared on MCT epilayers before ion implantation to avoid the external contamination and absorb the induced damages [17]. Here, the ZnS and CdTe films serve as barrier layers for MCT. Especially, the ZnS and CdTe double-layer films were grown on MCT epilayers by thermal evaporation as barrier layers, respectively, in order to investigate the influences of film materials and interface on arsenic profiles.

Figure 5(a) shows the SIMS profile of arsenic ions implanted into MCT coated by double-layer ZnS barrier layer (80 nm/80 nm) at 400 keV with the dose of 1×10^{14} cm^{-2}. Then, after removing the ZnS layer, the high-temperature annealing was performed at 420 and 240°C. The arsenic SIMS profile of the annealed sample is provided in **Figure 5(b)**. For the MCT sample covered with double-layer CdTe barrier layer (50 nm/100 nm), the arsenic ion implanted at 320 keV with the dose of 2×10^{14} cm^{-2}. In addition, the as-implanted sample was annealed in the same condition as the ZnS-coated sample after removing CdTe. The arsenic profiles of the MCT sample with CdTe barrier layer before and after annealing are illustrated in **Figure 6**. It can be seen that the arsenic ions are accumulated around the ZnS/MCT and ZnS/ZnS interfaces for the as-implanted ZnS-coated sample, and the peak concentration is located near the ZnS/MCT interface. For the as-implanted CdTe-coated sample, the arsenic ions are mainly accumulated at the CdTe/MCT interface. It indicates that the defects at the interface between barrier layer and MCT could serve as the trapping centers to

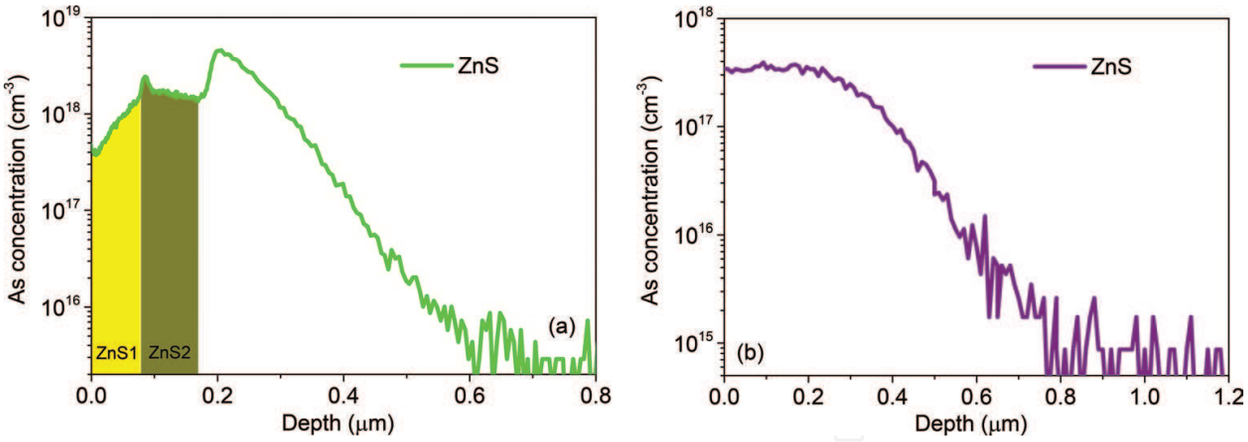


Figure 5. SIMS profile of arsenic ions implanted into MCT coated by double-layer ZnS barrier layer (80 nm/80 nm) at 400 keV with the dose of 1×10^{14} cm^{-2} (a) before annealing and (b) after annealing.

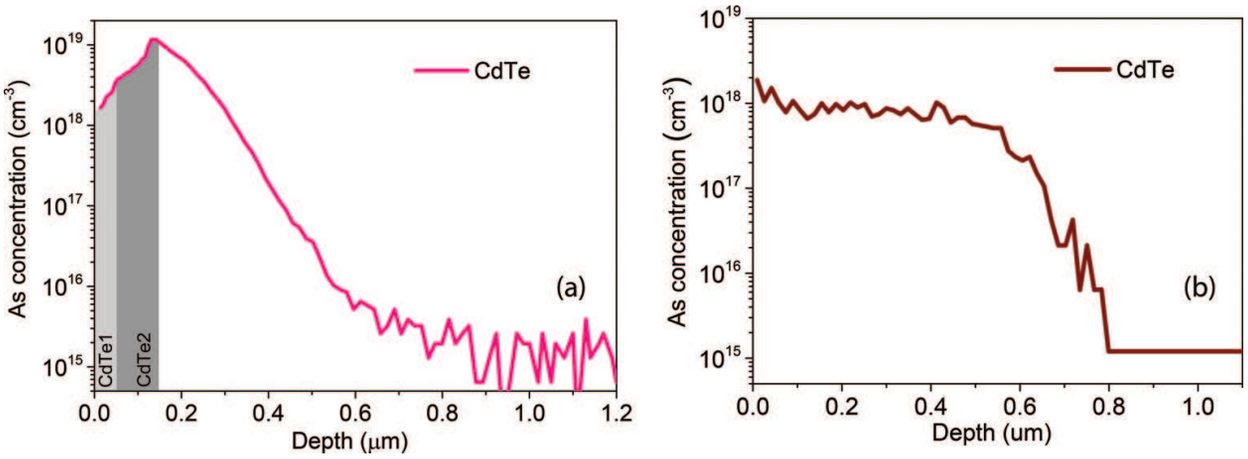


Figure 6. SIMS profile of arsenic ions implanted into MCT coated by double-layer CdTe barrier layer (50 nm/100 nm) at 320 keV with the dose of 2×10^{14} cm^{-2} (a) before annealing and (b) after annealing.

hinder arsenic ions. On the other hand, the shallower EOR depth of the ZnS-coated sample implanted with arsenic ions at higher energy shows that the ZnS layer has stronger barrier ability than CdTe.

2.2. Other dopants

Additionally, the profiles of the other group V dopants implanted into MCT were characterized by SIMS. **Figure 7** provides the SIMS profiles of phosphorus and antimony ions implanted into MCT epilayers, respectively. For phosphorus-implanted samples, the energy is 350 keV, the dose is 2×10^{14} cm^{-2}, and the beam currents are 50 and 800 μA. For antimony-implanted samples, the implant technological parameters are illustrated in **Figure 7(b)**. Dissimilar to arsenic, the phosphorus profiles are sensitive to the change in beam current. It can be seen that the EOR depth increases with beam current, which indicates that the extension of implantation

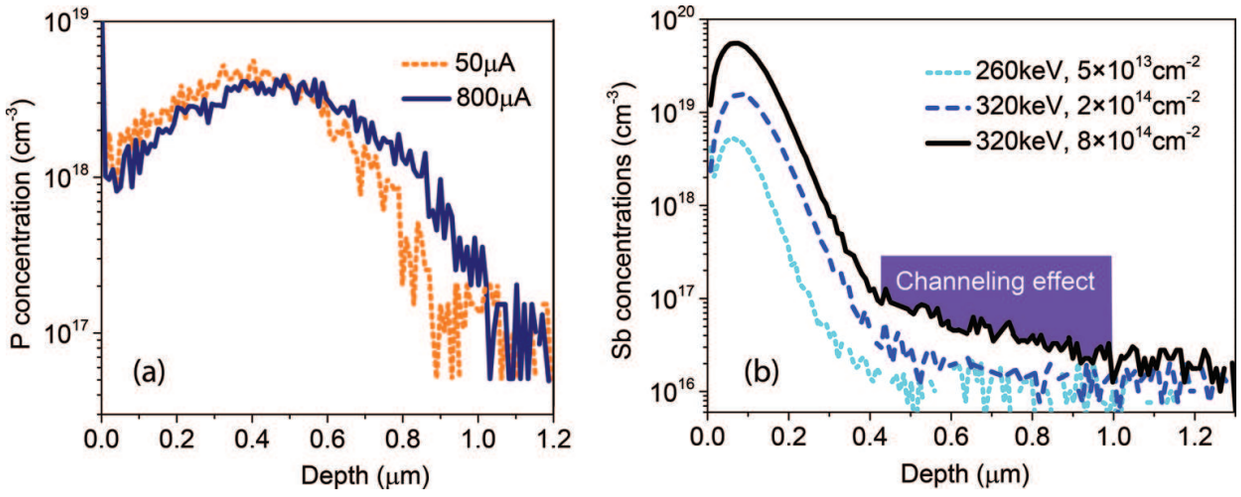


Figure 7. (a) SIMS profiles of phosphorus ions implanted into MCT epilayers at 350 keV with the dose of 2×10^{14} cm^{-2}, at the beam currents of 50 and 800 μA. (b) SIMS profiles of antimony ions implanted into MCT.

period for phosphorus ions, as a result of low beam current, gives rise to the increase in the interstitial ions. These interstitial ions could block the implantation of subsequent ions. By contrast, the motion of the arsenic ions implanted into MCT depends mainly on the displacements and replacements of lattice atoms through the collision between ions and atoms. For antimony-implanted samples, it is found that the high dose results directly in the channeling effect due to the large mass of antimony ions.

3. TEM characterization

So far, TEM is one of the most effective methods to characterize the microstructure of defects in materials. Next, the microstructures of the surface amorphization and induced defects in MCT epilayers implanted with arsenic and phosphorus ions will be characterized and analyzed by TEM.

3.1. Arsenic

Figure 8(a) and **(b)** provides the TEM cross-section images of near-surface layers in MCT implanted with arsenic ions at 350 and 450 keV, respectively. The dose is 2×10^{14} cm^{-2}. The arsenic profiles of these two samples have been given above. From the TEM observation, the induced damage layer can be divided into two sublayers: the amorphized-MCT (a-MCT) layer near surface, accompany with some long dislocations at the bottom; the short defect layer (SDL) with a large number of short defects. For the 350 keV sample, the thickness of the whole induced damage layer is about 0.45 μm. Therefore, the thicknesses of the a-MCT layer and the SDL are 0.28 and 0.17 μm, respectively. For the 450 keV sample, the whole damage layer is around 0.49 μm thick. Therefore, the thicknesses of the a-MCT layer and the SDL are 0.34 and 0.14 μm, respectively. It indicates that the induced damage to lattice for the sample implanted at higher

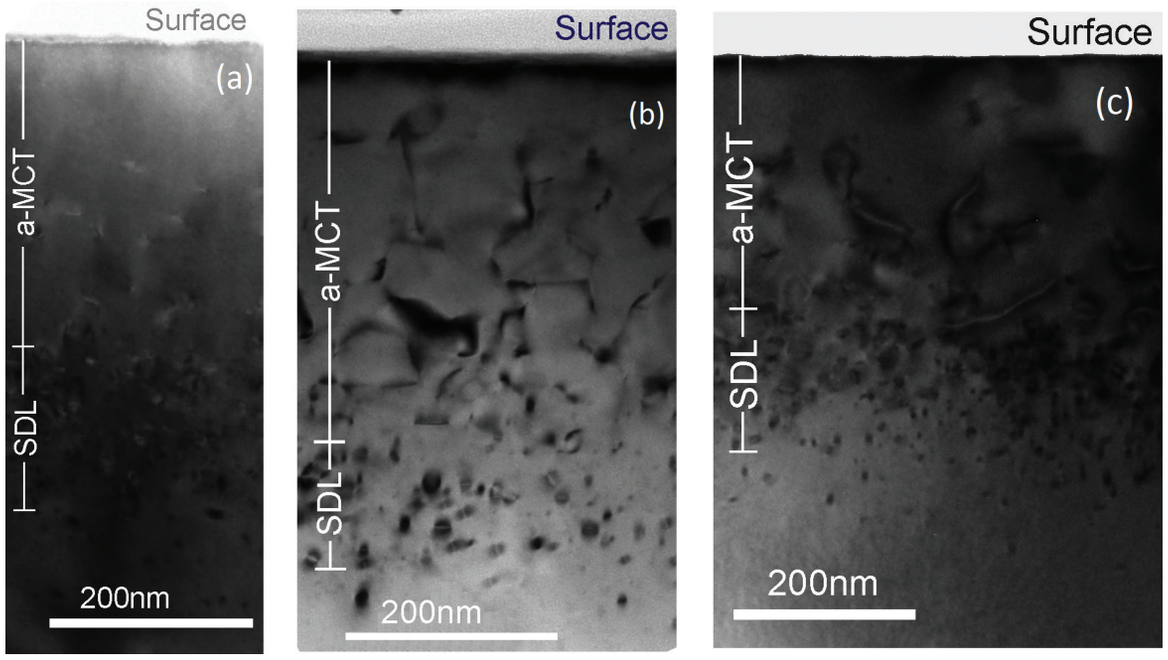


Figure 8. TEM cross-section images of near surface layers in MCT epilayers implanted with arsenic of 2×10^{14} cm^{-2} (a) at 350 keV, 50 μA; (b) at 450 keV, 50 μA; (c) at 350 keV, 800 μA.

energy is more serious than that of the sample implanted at lower energy. That is, the increase in implant energy results in the more energy transfer from implanted ions to lattice with the displacement of more lattice atoms, thereby aggravating the amorphization of surface MCT.

As mentioned earlier, the profiles of arsenic ions are insensitive to beam current. However, the change in beam current leads to the different distributions of induced damages. **Figure 8(c)** provides the TEM cross-section image of MCT implanted with arsenic of 2×10^{14} cm^{-2} at 350 keV and 800 μA. Compared with **Figure 8(a)**, the a-MCT layer and the SDL in the 50 μA sample are about 310 nm and 140 nm, respectively, while the 800 μA sample has a more thinner (260 nm) a-MCT layer and a thicker SDL layer (160 nm). Accordingly, the conclusion could be drawn that a longer period implantation at a low beam current could intensify the amorphization of the surface MCT.

Figure 9 provides the TEM cross-section images of the surface layers in MCT epilayers implanted with arsenic of 2×10^{14} and 5×10^{14} cm^{-2}, respectively. The implant energy is 320 keV. The thickness of the a-MCT layer in the low dose sample is less than that of the high dose sample, while the thickness of the SDL in the former is greater than that of the latter. It indicates that the longer period ion implantation equivalent to higher dose could prompt the amorphization of the surface MCT. Additionally, the insensitivity of the thickness of the whole damage layer to beam current implies that the SDL could be transformed to the a-MCT layer under the successive ion bombardment.

The high-resolution TEM was utilized to characterize the detailed microstructures of the induced defects in the SDL of arsenic-implanted MCT layers. As illustrated in **Figure 10**, the

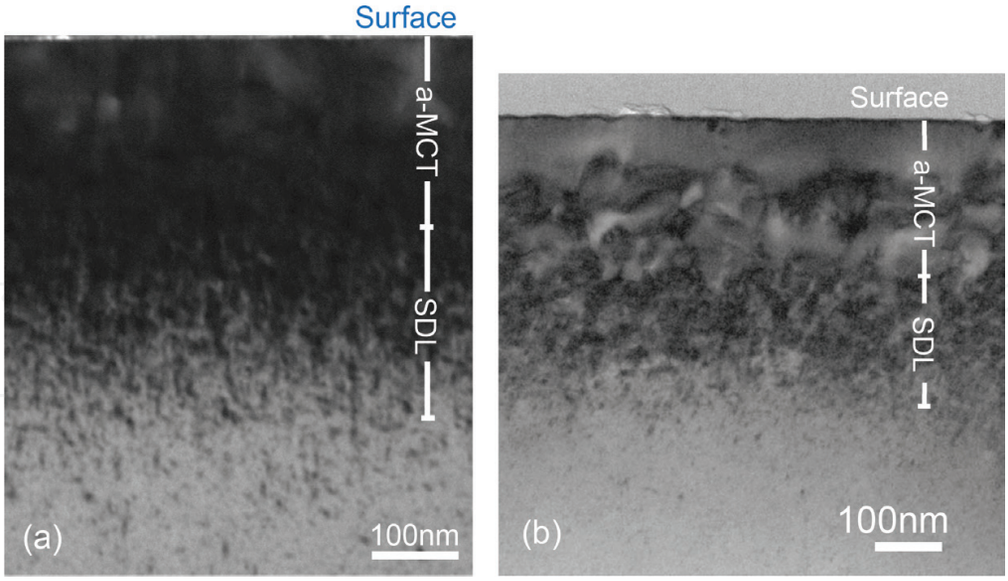


Figure 9. TEM cross-section images of the surface layers in MCT epilayers implanted with arsenic of (a) 2×10^{14} and (b) 5×10^{14} cm^{-2}, respectively, at 320 keV.

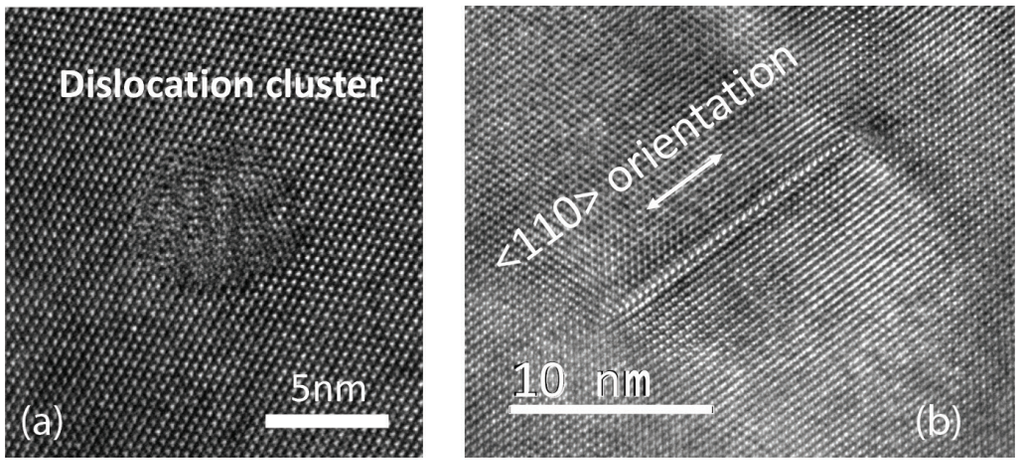


Figure 10. TEM images of induced defects in SDL of arsenic implanted MCT. (a) Dislocation cluster and (b) dislocation line.

short defects in the SDL could be classified into two types: dislocation cluster and dislocation line. Interestingly, most of dislocation lines are along <110> orientation parallel to the surface, which could be attributed to the larger atom spacing along the <110> orientation in MCT with the face-centered-cubic structure. Therefore, the recoil atoms induced by arsenic ions tend to be displaced along the <110> orientation to form dislocation lines.

Specially, the residual defects were discovered around the previous interface between a-MCT layer and SDL for the arsenic implanted MCT at 450 keV after Hg overpressure annealing, forming a belt of point defects, as shown in **Figure 11**. It indicates that the induced defects formed at adequately high implant energy could not be eliminated even after annealing.

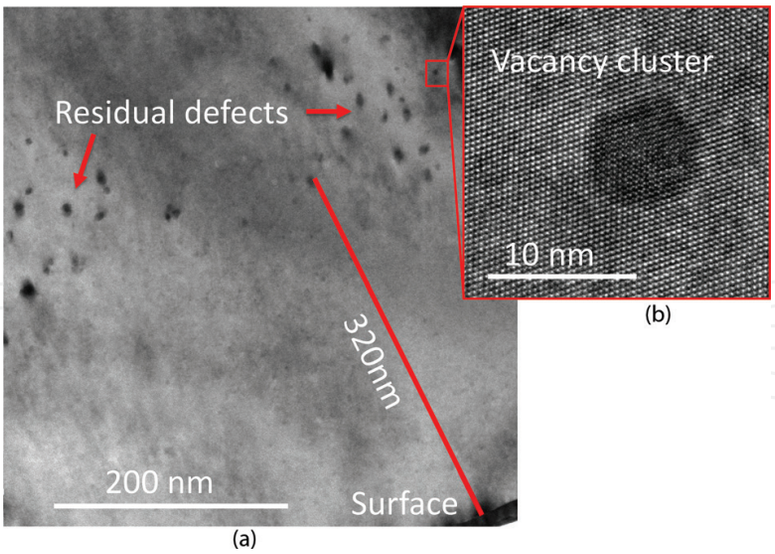


Figure 11. (a) TEM image of a belt of residual point defects in MCT epilayer implanted with arsenic ions at 450 keV after Hg overpressure annealing. (b) Detailed TEM image of residual point defect.

In order to characterize the details of these residual defects, the high-resolution TEM was adopted. It can be seen from the insert chart in **Figure 11** that the point defect is actually a cluster of vacancies. The deduction could be acquired that the ion implantation at too high energy will result in the net loss of lattice atoms.

The barrier layer is deposited to protect the MCT epilayer from the external contamination and absorb the induced damages. However, the thin evaporated CdTe barrier layer was proved to generate the BLICE effect [13]. This effect can be suppressed by increasing the thickness of evaporated CdTe layer and adopting the other barrier layer materials [12]. Here, the TEM cross-section images of the double-layer ZnS-coated MCT epilayer (implanted with arsenic at 400 keV) and the double-layer CdTe-coated MCT epilayer (implanted with arsenic at 320 keV) are provided in **Figure 12** respectively. The a-MCT layers become very thin or almost disappear both in the MCT epilayers of the two samples. In addition, the thinner SDL in the ZnS-coated sample implanted at higher energy demonstrates the stronger barrier effect of ZnS than CdTe. The thickness of the barrier layer can be optimized to adjust the SDL depth.

3.2. Other dopants

The microstructure and distribution of induced defects in the MCT epilayer implanted with the other group V dopants such as phosphorus were also characterized by TEM as illustrated in **Figure 13**. The thicknesses of the a-MCT layer and the SDL in the phosphorus-implanted sample are about 380 and 220 nm, respectively. Obviously, the induced damages of implanted phosphorus ions to lattice are more serious than arsenic ions under the same implantation condition, compared with **Figure 8(a)**. Moreover, in addition to dislocation cluster and dislocation line, the crescent dislocation is discovered in the SDL of phosphorus implanted MCT as shown in **Figure 13(b)**.

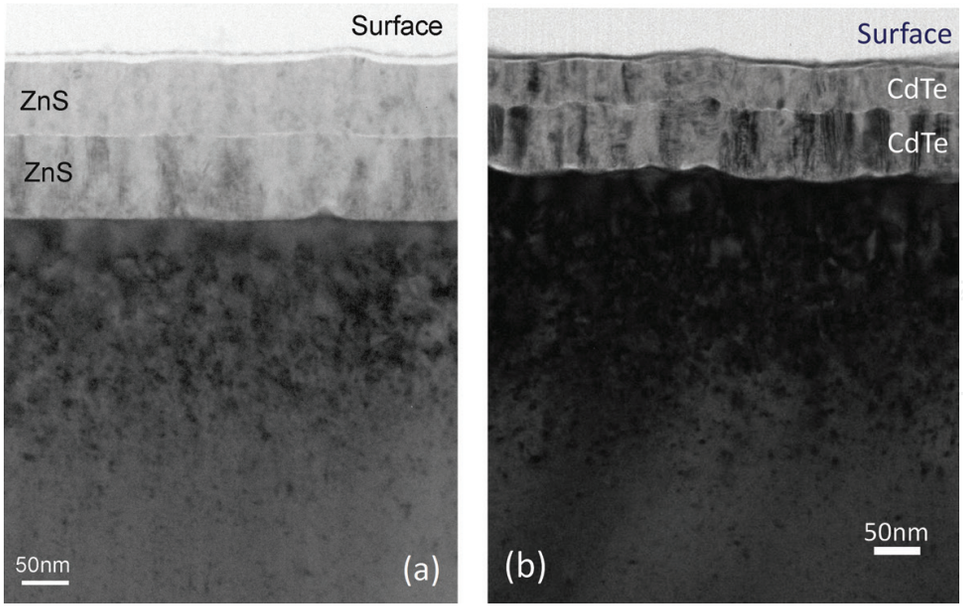


Figure 12. (a) TEM cross-section images of the double-layer ZnS-coated MCT epilayer implanted with arsenic at 400 keV. (b) TEM cross-section images of the double-layer CdTe-coated MCT epilayer implanted with arsenic at 320 keV.

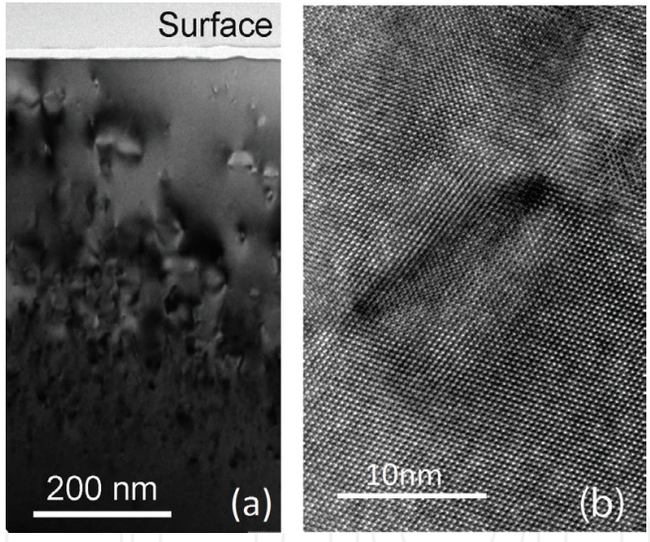


Figure 13. (a) TEM cross-section image of the near surface layer in the MCT epilayer implanted with phosphorus ions of 2×10^{14} cm^{-2} at 350 keV. (b) TEM image of a crescent dislocation in the SDL of the phosphorus-implanted MCT.

4. XRD analysis

XRD usually serves as an analytic method of characterizing the crystallinity and the preferred orientation of materials. Here, it is utilized to characterize the change in the lattice structure of as-implanted MCT epilayers. **Figure 14** illustrates the characteristic diffraction peaks of un-implanted, arsenic implanted, and phosphorus implanted MCT epilayers. It can be seen that the characteristic peak of the un-implanted epilayer is symmetric and the full width at

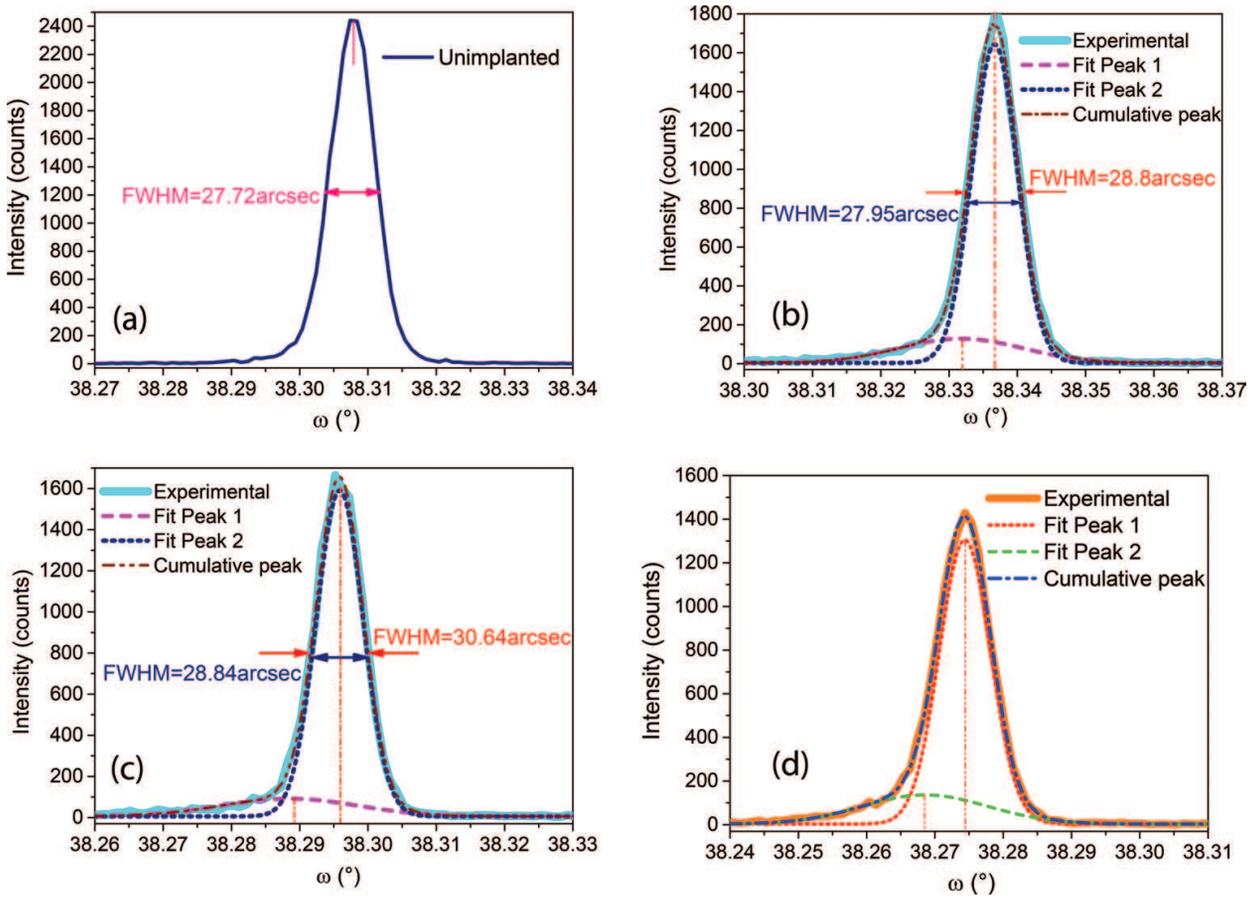


Figure 14. Characteristic diffraction peaks of (a) un-implanted MCT layer, (b) MCT layer implanted with arsenic ions of 2×10^{14} cm^{-2} at 350 keV, (c) MCT layer implanted with arsenic ions of 2×10^{14} cm^{-2} at 450 keV and (d) MCT layer implanted with phosphorus ions of 2×10^{14} cm^{-2} at 450 keV.

half maximum (FWHM) is about 27.7 arcsec. Subjected to ion implantation, the FWHMs of the characteristic peaks of as-implanted MCT epilayers are all broadened. Under the same implant condition, the FWHM of the arsenic implanted sample increases from 27.7 arcsec to 28.8 arcsec, while the FWHM of the phosphorus implanted sample increases from 27.7 arcsec to 33.1 arcsec. Moreover, these peaks become asymmetrical and can be decomposed into two subpeaks by multipeak fitting: a narrow peak with a lower intensity and a broad peak with a very low intensity. The broad peak moves in the direction of the angle ω reduction. It demonstrates that the surface MCT material is amorphized and the corresponding lattice constant increases. Therefore, the FWHM and the position of the broad peak are related to the amorphization of the surface MCT layer. In addition, the position offset and the intensity of the broad peak relative to the cumulative peak should be used to describe the level of amorphization in near surface layer of MCT.

5. Computer simulation

The characterization of ion profiles and induced defects in the MCT epilayers implanted with group V dopants was discussed and analyzed above. Here, some simulation results of

implanted ion trajectories and recoil atom motions in bare and barrier layer-coated MCT epilayers are presented based on the calculation of computer software.

In fact, the trajectories of implanted ions in lattice are random and unrepeatable as shown in **Figure 15(a)**. A number of continuous collisions between an implanted ion and lattice atoms occur, and the ion can stop at a certain position in the lattice. Moreover, the recoil atoms struck by the implanted ion could result in the collision cascades with the other lattice atoms, thereby generating more recoil atoms. The distribution of the recoil atoms corresponding to the ion trajectories in **Figure 15(a)** is illustrated in **Figure 15(b)**. It can be seen that the distribution region of recoil atoms is layer than that of ion trajectories. Therefore, the origin of the induced damages can be considered to be the collision cascade of recoil atoms. On the other hand, both the distributions of ion trajectories and recoil atoms are isotropic for bare MCT implanted with ions. That is, the net loss of lattice atoms could occur due to the short projected range of implanted ions in MCT.

Figure 16 provides the linear density of implanted arsenic and phosphorus ions versus the MCT target depth with the implant energy of 350 keV. From this diagram, the average projected range (R_p) and the ion peak linear density can be acquired. Here, the peak linear densities of arsenic and phosphorus ions are approximately 5×10^4 (at./cm^3)/(at./cm^2) and 2.4×10^4 (at./cm^3)/(at./cm^2), respectively. Calculating with the implant dose of 2×10^{14} cm^{-2} from the samples shown in **Figures 1(a)** and **7(a)**, the theoretical peak concentrations of implanted arsenic and phosphorus ions should be estimated to be ~1×10^{19} cm^{-3} and ~4.8×10^{18} cm^{-3}, respectively, in accordance with the measured peak concentrations of arsenic ions in **Figure 1(a)** and phosphorus ions in **Figure 7(a)**. Therefore, the simulation results should be credible for theoretically calculating the distributions of implanted ions and recoil atoms.

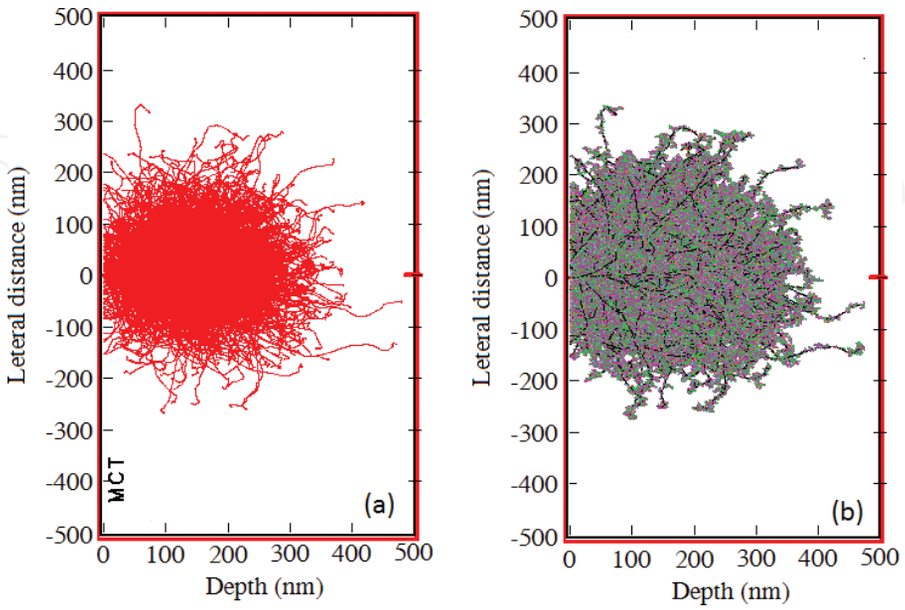


Figure 15. Simulated distributions of (a) ion trajectories and (b) recoil atoms in the bare MCT implanted with arsenic ions at 350 keV based on the computer software.

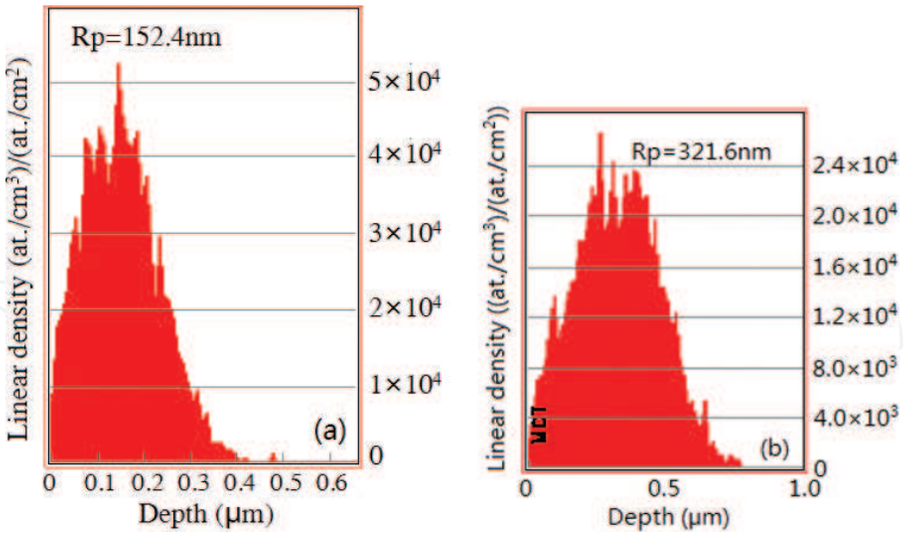


Figure 16. Linear density of implanted arsenic and phosphorus ions versus the MCT target depth with the implant energy of 350 keV acquired from computer simulation. (a) Arsenic ions and (b) phosphorus ions.

Figure 17 shows the histogram of the simulation and experimental values of average projected ranges (Rp) of arsenic, phosphorus, and antimony ions implanted into bare MCT epilayers at different energies. It can be seen that the simulation results are in good agreement with the experimental values. The light ion (P) possesses the largest Rp values, while the heavy ion (Sb) has the smallest Rp values. Additionally, the Rp value increases approximately linearly with implant energy.

Subsequently, the ion trajectories and the recoil atom motions in the MCT epilayers covered by ZnS and CdTe double-layer barrier layers implanted with arsenic ions were simulated, respectively. In the simulation, the density of the evaporated ZnS film is selected to be about 3.3 g/cm^3 [18], while the density of the evaporated CdTe film is set to be 5.83 g/cm^3 [19]. **Figure 18** provides the ion

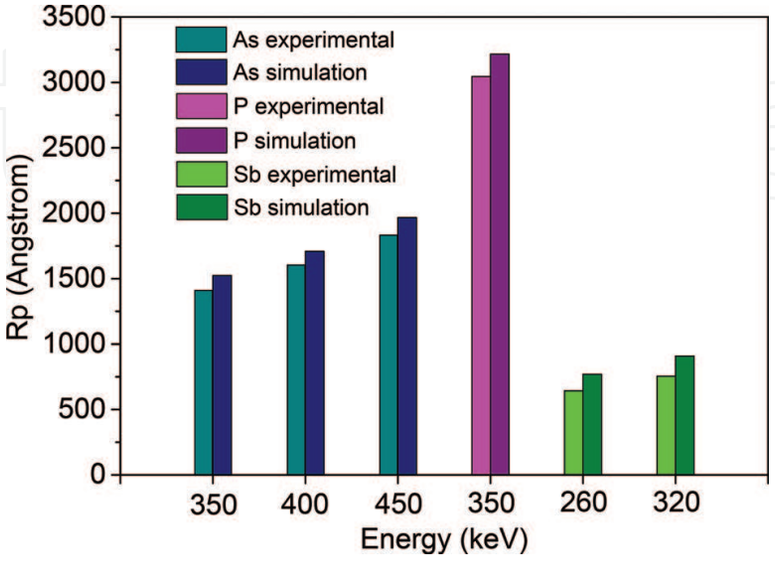


Figure 17. Histogram of the simulation and experimental values of average projected ranges (Rp) of arsenic, phosphorus and antimony ions implanted into bare MCT epilayers at different energies: As~350, 400 and 450 keV; P~350 keV; Sb~260 and 320 keV.

trajectories of arsenic ions implanted into ZnS-coated and CdTe-coated MCT targets, respectively. It should be noted that the ion trajectories in the ZnS-coated sample appear to be a little anisotropic, while the ion trajectories in the CdTe-coated sample are still isotropic, similar to bare MCT.

The linear densities of arsenic ions implanted into the MCT covered by ZnS and CdTe barrier layers are illustrated in **Figure 19**. It can be seen that the peak linear densities of arsenic ions in these two targets are both close to the interface between barrier layer and MCT. The peak linear densities of arsenic ions in the ZnS-coated and CdTe-coated samples are approximately 5.5×10^4 (at./cm^3)/(at./cm^2) and 5.6×10^4 (at./cm^3)/(at./cm^2), respectively. Calculating with the dose of 1×10^{14} cm^{-2} from the sample shown in **Figure 5(a)** and the dose of 2×10^{14} cm^{-2} from the sample shown in **Figure 6(a)**, the theoretical peak arsenic concentrations in the ZnS-coated and CdTe-coated samples should be estimated to be ~5.5×10^{18} and ~1.1×10^{19} cm^{-3}, respectively, very close to the measured peak concentrations of ~4.9×10^{18} cm^{-3} in **Figure 5(a)** and ~1.15×10^{19} cm^{-3} in **Figure 6(a)**. **Figure 20** provides the histogram of the simulation and experimental Rp values of arsenic ions implanted into the ZnS-coated and CdTe-coated MCT epilayers, with good consistency between the simulation values and the experimental values.

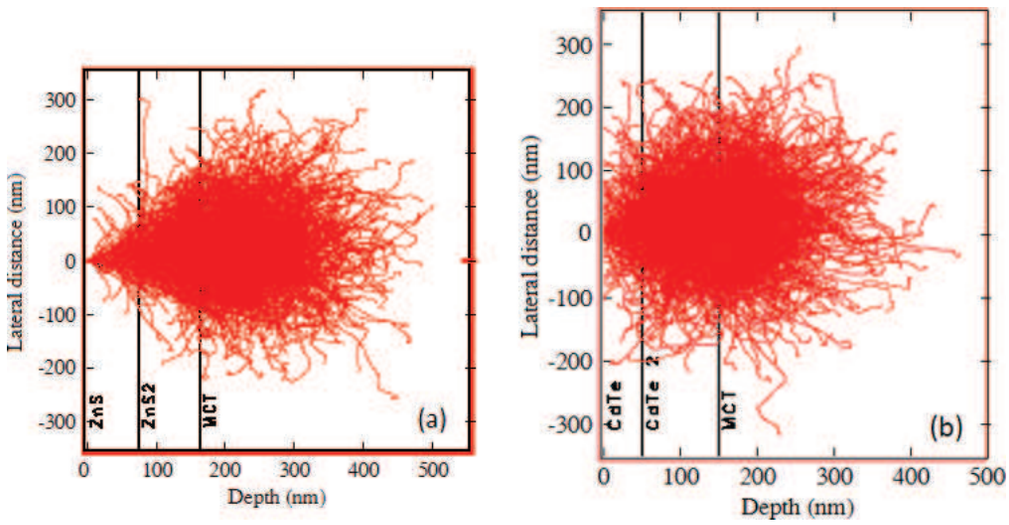


Figure 18. Ion trajectories of arsenic ions implanted into (a) ZnS-coated (implant energy ~ 400 keV) and (b) CdTe-coated (implant energy ~ 320 keV) MCT targets, respectively.

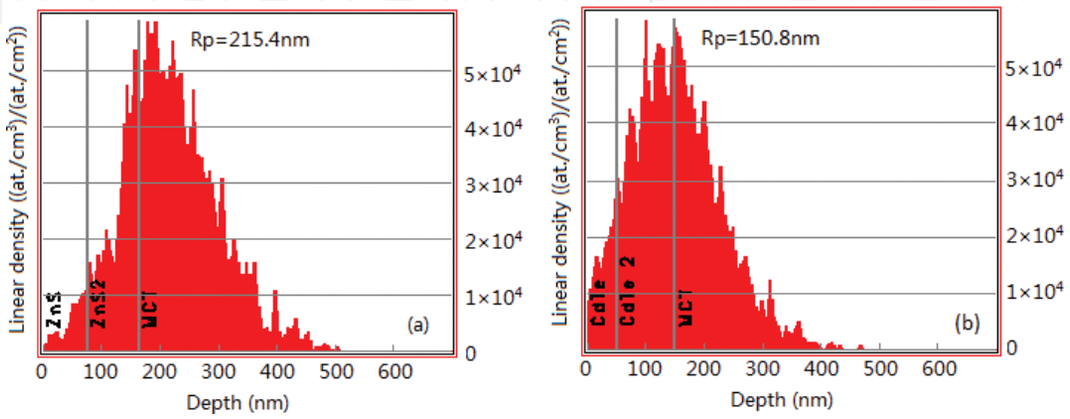


Figure 19. Linear densities of arsenic ions implanted into (a) ZnS-coated (implant energy ~ 400 keV) and (b) CdTe-coated (implant energy ~ 320 keV) MCT targets, respectively.

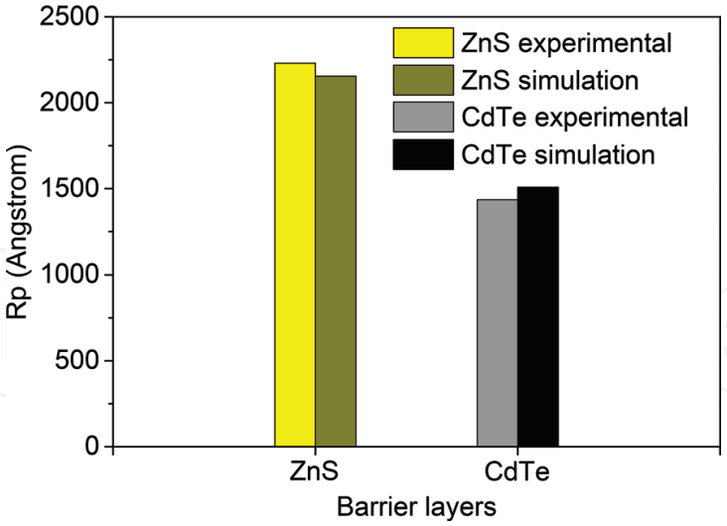


Figure 20. Histogram of the simulation and experimental Rp values of arsenic ions implanted into the ZnS-coated and CdTe-coated MCT epilayers.

6. Conclusion

In this chapter, the p-type (As, P and Sb) ion implantation in MCT epilayer is investigated based on the characterization methods such as SIMS, TEM and XRD. The distribution profiles of arsenic, phosphorus and antimony ions implanted into MCT were measured by SIMS. The influences of some key technological parameters, including energy, dose and beam current, on the distribution and diffusion of implanted ions were discussed and analyzed. Meanwhile, the microstructures of surface amorphization and induced defects in as-implanted MCT were characterized by TEM. The short defects in SDL include dislocation cluster, dislocation line and crescent dislocation. Moreover, the residual point defect belt comprised with vacancy clusters was observed to prove the occurrence of the net loss of lattice atoms under the ion bombardment of too high energy. In addition, XRD was utilized to characterize the variance of lattice structure induced by ion implantation. The position offset of the broad diffraction sub-peaks and the FWHM broadening of the cumulative peaks are attributed to the surface amorphization of as-implanted epilayers. As an important technological structure, the effects of the barrier layers, such as ZnS, CdTe, on the ion profiles and induced defect distributions are studied. Finally, the ion trajectories and recoil atom motions in bare and barrier layer-coated MCT targets were simulated based computer software. The average projected ranges and the peak doping concentrations were calculated theoretically, with good consistency with the experimental values.

Acknowledgements

This work is supported by Innovation Special Fund from Shanghai Institute of Technical Physics (Q-DX-58, Q-DX-84).

Thanks

The author wishes to thank the staff of Research Center for Advanced Materials and Devices at Shanghai Institute of Technical Physics where the sample preparation was completed. Thanks to Prof. Yanfeng Wei for supplying LPE MCT epilayers, and Engineer Chao Yang for ion implantation operation. Special thanks to my mother, Mrs. Xianglan Zhao, for life care and spiritual support.

Author details

Changzhi Shi

Address all correspondence to: shichangzhi@mail.sitp.ac.cn

Research Center for Advanced Materials and Devices, Shanghai Institute of Technical Physics, Chinese Academy of Sciences, Shanghai, China

References

[1] Saur W. Long wavelength mercury-cadmium telluride photoconductive infrared detectors. Infrared Physics. 1968;**8**(3):255-258. DOI: 10.1016/0020-0891(68)90016-X

[2] Wollrab R, Bauer A, Bitterlich H, Bruder M, Hanna S, Lutz H, Mahlein K-M, Schallenberg T, Ziegler J. Planar n-on-p HgCdTe FPAs for LWIR and VLWIR applications. Journal of Electronic Materials. 2011;**40**(8):1618-1623. DOI: 10.1007/s11664-011-1659-0

[3] Gravrand O, DE Borniol E, Bisotto S, Mollard L, Destefanis G. From long infrared to very long infrared wavelength focal plane arrays made with HgCdTe n+n−/p ion implantation technology. Journal of Electronic Materials. 2007;**36**(8):981-987. DOI: 10.1007/s11664-007-0151-3

[4] Bubulac LO, Lo DS, Tennant WE, Edwall DD, Chen JC, Ratusnik J, Robinson JC, Bostrup G. p On n ion-implanted junctions in liquid phase epitaxy HgCdTe layers on CdTe substrates. Applied Physics Letters. 1987;**50**(22):1586-1588. DOI: 10.1063/1.97788

[5] Cooper DE, Harrison WA. Possible negative-U properties of the cation vacancy in HgCdTe. Journal of Vacuum Science & Technology A. 1990;**8**(2):1112-1115. DOI: 10.1116/ 1.576970

[6] Kinch MA, Aqariden F, Chandra D, Liao P-K, Schaake HF, Shih HD. Minority carrier lifetime in p-HgCdTe. Journal of Electronic Materials. 2005;**34**(6):880-884. DOI: 10.1007/s11664-005-0036-2

[7] Rogalski A. HgCdTe infrared detector material: History, status and outlook. Reports on Progress in Physics. 2005;**68**:2267-2336. DOI: 10.1088/0034-4885/68/10/R01

[8] Mollard L, Destefanis G, Baier N, Rothman J, Ballet P, Zanatta JP, Tchagaspanian M, Papon AM, Bourgeois G, Barnes JP, Pautet C, Fougeres P. Planar p-on-n HgCdTe FPAs by arsenic ion implantation. Journal of Electronic Materials. 2009;**38**(8):1805-1813. DOI: 10.1007/s11664-009-0829-9

[9] Mollard L, Bourgeois G, Lobre C, Gout S, Viollet-Bosson S, Baier N, Destefanis G, Gravrand O, Barnes JP, Milesi F, Kerlain A, Rubaldo L, Manissadjian A. P-on-n HgCdTe infrared focal-plane arrays: From short-wave to very-long-wave infrared. Journal of Electronic Materials. 2014;**43**(3):802-807. DOI: 10.1007/s11664-013-2809-3

[10] Baier N, Cervera C, Gravrand O, Mollard L, Lobre C, Destefanis G, Bourgeois G, Zanatta JP, Boulade O, Moreau V. Latest developments in long-wavelength and very-long-wavelength infrared detection with p-on-n HgCdTe. Journal of Electronic Materials. 2015;**44**(9):3144-3150. DOI: 10.1007/s11664-015-3851-0

[11] Mollard L, Destefanis G, Bourgeois G, Ferron A, Baier N, Gravrand O, Barnes JP, Papon AM, Milesi F, Kerlain A, Rubaldo L. Status of p-on-n arsenic-implanted HgCdTe technologies. Journal of Electronic Materials. 2011;**40**(8):1830-1839. DOI: 10.1007/s11664-011-1692-z

[12] Shi C-Z, Lin C, Wei Y-F, Chen L, Ye Z-H. Influences of thicknesses and structures of barrier cap layers on As ion profiles and implant damages in HgCdTe epilayers. In: Proceedings of Infrared Technology and Applications XLII; April 17-21, 2016. Baltimore: SPIE; 2016. p. 981923-1-7

[13] Shi C-Z, Lin C, Wei Y-F, Chen L, Zhu M-X. Barrier layer induced channeling effect of As ion implantation in HgCdTe and its influences on electrical properties of p–n junctions. Applied Optics. 2016;**55**(34):D101-D105. DOI: 10.1364/AO.55.00D101

[14] Shi C-Z, Lin C, Wei Y-F, Chen L. Microstructure characterization of lattice defects induced by As ion implantation in HgCdTe epilayers. In: Proceedings of Infrared Technology and Applications XLIII; April 9-13, 2017. Anaheim: SPIE; 2017. p. 101771C-1-5

[15] Lobre C, Jalabert D, Vickridge I, Briand E, Benzeggouta D, Mollard L, Jouneau PH, Ballet P. Quantitative damage depth profiles in arsenic implanted HgCdTe. Nuclear Instruments and Methods in Physics Research Section B. 2013;**313**:76-80. DOI: 10.1016/j.nimb.2013.07.019

[16] Lobre C, Jouneau P-H, Mollard L, Ballet P. Characterization of the microstructure of HgCdTe with p-type doping. Journal of Electronic Materials. 2014;**43**(8):2908-2914. DOI: 10.1007/s11664-014-3147-9

[17] Ye ZH, Huang J, Yin W-T, Hu W-D, Feng J-W, Chen L, Liao Q-J, Chen H-L, Lin C, Hu X-N, Ding R-J, He L. HgCdTe photodiode arrays passivated by MBE in-situ grown CdTe film. Journal of Infrared, Millimeter, and Terahertz Waves. 2011;**30**(6):495-498. DOI: 1001-9014(2011) 06-0495-05

[18] Bessergenev VG, Ivanova EN, Kovalevskaya YA, Gromilov SA, Kirichenko VN, Zemskova SM, Vasilieva IG, Ayupov BM, Shwarz NL. Optical and structural properties of ZnS and ZnS:Mn films prepared by CVD method. Materials Research Bulletin. 1995;**30**(11):1393-1400. DOI: 0025-5408(95)00150-6

[19] Gschwendtner E, Placidia M, Schmicklera H. Polycrystalline CdTe detectors: A luminosity monitor for the LHC. Nuclear Physics B – Proceedings Supplements. 2003;**125**:363-367. DOI: S0920-5632(03)91017-6